Optical and Quantum Electronics (2019) 51:192
https://doi.org/10.1007/s11082-019-1913-x

Optical and photoluminensce properties of Eu^{2+}-activated strontium magnesium silicate phosphors using different rare earth co-activators

M. M. S. Sanad[1] · D. A. Rayan[1] · M. M. Rashad[1]

Received: 29 October 2018 / Accepted: 24 May 2019 / Published online: 27 May 2019

Abstract
Nanostructured powders of $Sr_{1.96}MgSi_2O_7{:}Eu^{2+}_{0.01}$, $R^{3+}_{0.01}$ ($R^{3+}=Er^{3+}$, Tm^{3+} and Tb^{3+}) have been fabricated via urea combustion technique. XRD results implied that tetragonal $Sr_2MgSi_2O_7$ was the major phase whereas monoclinic Sr_2SiO_4 and $SrSiO_3$ were the minor phases. Meanwhile, field emission SEM textures showed the hollow spherical network-like shape structures filled with fused interconnections for the $Sr_{1.96}MgSi_2O_7{:}Eu^{2+}_{0.01}$ sample. It has been recognized that the replacement of Sr^{2+} with co-dopant R^{3+} ions e.g. Er^{3+}, Tm^{3+} and Tb^{3+} considerably help obtaining homogeneous structure as well. The values of band gap energy and calculated refractive index were ultimately dependant on the ionic radius of R^{3+} co-doping ion. It has been suggested that the divalent activator ion (Eu^{2+}) was responsible for the number of PL emission spectra, while the trivalent co-activator ions (R^{3+}) were the key reasons for variations in the broadening and intensity of PL emission spectra.

Keywords Silicate based phosphors (A) · Combustion process (B) · Cell parameters (c) · Crystal morphology (D) · Luminescent phosphors (D)

1 Introduction

Alkaline earth silicate based phosphors have attracted much attention as host materials than can display distinguished luminescence properties compared with aluminate and sulphide based phosphors (Yu et al. 2004; Fu et al. 2005; Clabau et al. 2005; Gong et al. 2012). In this context, Eu^{2+}-activated strontium magnesium silicate (SMS) phosphors have been potentially utilized for various applications such as decorative paints, traffic and emergency signs, photo-sensitizers, biological probes and medical diagnostics (Chen et al. 2006; Wu et al. 2011; Maldiney et al. 2013). The most commonly Eu^{2+}, Dy^{3+}-codoped strontium magnesium silicate material has been extensively considered, suggesting excellent properties of chemical stability, high quantum efficiency and long afterglow brightness (i.e. phosphorescence) (Pan et al. 2008; Song et al. 2008; Wu et al. 2010, 2011; Ishizaki et al. 2012;

✉ M. M. Rashad
rashad133@yahoo.com

[1] Central Metallurgical R & D Institute (CMRDI), P.O. Box 87, Helwan, Cairo, Egypt

Ye et al. 2013). Basically, the co-activator (codopant ion) plays a crucial role in harnessing the emission extent and prolonging the decay time by trapping the free holes and allowing multiple electronic 4f–5d transitions between the produced successive energy levels (Chen et al. 2006; Dorenbos 2005; Aitasalo et al. 2006; Shi et al. 2007). In this regard, a lot of research has been accomplished during the last few years concentrated on exploring the effect of different divalent activators such as Eu^{2+}, Mn^{2+} and trivalent co-activators such as Dy^{3+}, Tm^{3+}, La^{3+} and Nd^{3+}, … etc. on the luminescence emission properties of alkaline earth silicate based host materials (Aitasalo et al. 2005; Liu et al. 2005; Wu et al. 2009, 2010; Alvani et al. 2005). Moreover, various preparation methods have been introduced for synthesis of the long persistent activated strontium magnesium silicate phosphors including solid state (Gong et al. 2012; Song et al. 2008; Li et al. 2009), co-precipitation (Pan et al. 2008), combustion (Bhatkar and Bhatkar 2011) and spinning processes (Ye et al. 2013; Jun et al. 2014). Otherwise, there is a significant lack in the research studies concerning the impact of co-dopant (i.e. co-activator) ions rather than Dy^{3+} ion which are mainly responsible for the afterglow phenomena of all photoluminescence materials. The recent study of different co-activators e.g. Er^{3+}, Tm^{3+} and Tb^{3+} on Eu^{2+}-$SrAl_2O_4$ has confirmed the fundamental differences in the photoluminescence effect with each lanthanide cations (Sanad and Rashad 2016). For these reasons, this work aims at monitoring the principal changes in the crystallographic, morphological, optical and photoluminescence properties of Eu^{2+}-$Sr_2MgSi_2O_7$ samples and the Eu^{2+}, R^{3+}co-activated samples with different lanthanide cations including Er^{3+}, Tm^{3+} and Tb^{3+}. Accordingly, nano-structured phosphors powders have been synthesized via simple urea combustion method. Alongside, different parameters such as cell parameters, particle size, band energy gap as well as refractive index and emission spectrum maxima have determined from the obtained results.

2 Experimental

2.1 Materials and methods

Anhydrous strontium nitrate $Sr(NO_3)_2$ (Sigma-Aldrich 99.9%), magnesium acetate tetrahydrate $Mg(OAc)_2.4H_2O$ (Sigma-Aldrich 99.9%), TEOS $SiC_8H_{20}O_4$ (Sigma-Aldrich 99.9%), europium nitrate hexahydrate $Eu(NO_3)_3.6H_2O$ (Alfa Aesar 99.9%), erbium acetate tetrahydrate $Er(OAc)_3.4H_2O$ (Alfa Aesar 99.9%), thulium acetate hydrate $Tm(OAc)_3.xH_2O$ (Sigma-Aldrich 99.9%), terbium nitrate pentahydrate $Tb(NO_3)_3.5H_2O$ (Sigma-Aldrich 99.9%) and urea N_2H_4CO (Sigma-Aldrich 99.5%) were employed as raw materials. Deionized water was used in the whole work. Strontium magnesium silicate phosphors of four chemical compositions $Sr_{1.99}MgSi_2O_7$:$Eu^{2+}_{0.01}$ (SMS1), $Sr_{1.98}MgSi_2O_7$:$Eu^{2+}_{0.01}$, $Er^{3+}_{0.01}$ (SMS2), $Sr_{1.98}MgSi_2O_7$:$Eu^{2+}_{0.01}$, $Tm^{3+}_{0.01}$ (SMS3) and $Sr_{1.98}MgSi_2O_7$:$Eu^{2+}_{0.01}$,$Tb^{3+}_{0.01}$ (SMS4) microporous samples were synthesized via urea combustion method. In typical synthesis, Sr, Mg, Si and Eu (1%wt.) salts of stoichiometric amounts were dissolved in 0.5 M urea solution which act as a combustion fuel and complexing agent. Then, about 1%wt of R^{3+} (Er^{3+}, Tm^{3+} or Tb^{3+}) salts was also added for precursor preparation of the codoped strontium magnesium silicate phosphors $Sr_{1.98}MgSi_2O_7$: Eu^{2+}, R^{3+}. The solutions were mixed for 30 min then boiled to evaporate the excess water. Thereafter, the resulting viscous liquid started to undergo auto-combustion after putting the glass beaker directly in a muffle furnace (at 400 °C) yielding grayish dark fluffy precursor powders. Finally, the obtained combustion precursors were pre-calcined at 1000 °C for 6 h in an air atmosphere to remove the

residual carbon. Finally, these powders were calcined again at 1200 °C for 3 h with heating rate (5° min^{-1}) in presence of gas mixture (argon 95% and hydrogen 5%). The reducing H_2 gas of 5% was injected in order to ensure complete conversion of activator ion Eu^{3+} into Eu^{2+} ion.

2.2 Sample characterization

X-ray powder diffraction (XRD) was executed on a model Bruker AXS diffractometer (D8-ADVANCE Germany) with Cu Kα ($\lambda = 1.54056$ Å) radiation, operating at 40 kV and 40 mA. The diffraction data were recorded for 2θ values between 20° and 60° and the scanning rate was 3° min^{-1} or 0.02°/0.4 s). The particle morphology was inspected by a field emission scanning electron microscopy FE-SEM (JEOL-JSM-5410 Japan). The optical measurements were implemented using (Jasco-V-570 spectrophotometer, Japan) using integrating sphere reflectance unit. The diffuse reflectance and absorption spectrum measurements of all phosphors have been accomplished in the wavelength range 200-2000 nm at room temperature. Photoluminescence (PL) spectra were obtained at room temperature using fluorescence spectrophotometer (SHIMADZU RF-5301PC Japan) with xenon discharge lamp (150 W) as excitation source.

3 Results and discussion

3.1 Crystal structure

Figure 1a shows the XRD patterns of Eu^{2+}-doped and Eu^{2+}, R^{3+} -codoped samples calcined at 1200 °C for 3 h. The $Sr_2MgSi_2O_7$ tetragonal crystal structure is clearly identified as the major phase (PDF card no. 75-1736) with P-42_{1m} space group. Minor diffraction peaks are also detected for two phase impurities including Sr_2SiO_4 (PDF card no. 39-1256) and $SrSiO_3$ (PDF card no. 24-1230) phases where they could be obtained as a result of

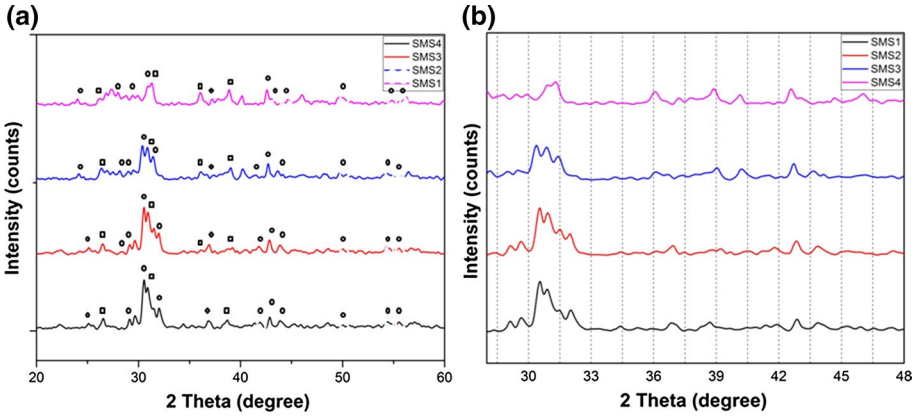

Fig. 1 **a** XRD patterns of SMS, SMS2, SMS3 and SMS4 phosphor powders prepared at1200 °C, $Sr_2MgSi_2O_7$ (circle), Sr_2SiO_4 (square) and $SrSiO_3$ (diamond), **b** Grid profile of all XRD patterns to show the peaks shift

replacing Sr^{2+} with two types of rare earth ions. Therefore, the crystallinity and peaks intensities of the main phase are quite depressed in case of SMS3 and SMS4 codoped samples. It is also noticed that the peaks of the main phase are slightly shifted which considered a true evidence of rare earth ions introduction in the crystallite sites of Sr^{2+} ions as shown in Fig. 1b. The detected broadening for most of XRD peaks suggests the nano-sized crystals of the prepared powders. Evidently, the crystallite size of $Sr_2MgSi_2O_7$ phase in the as-prepared nanocomposites can be estimated by applying Scherrer's equation (Sanad et al. 2014) based on the average of the highest two reflections (211) at $2\theta = 30.5°$ and (212) at $2\theta = 43.3°$ using the full width at half maximum (FWHM). It is found that the Eu^{2+}, R^{3+}-codoped samples have smaller crystallite sizes than that of Eu^{2+}-doped sample. This might be explained by the crystallinity quenching with rare earth elements which has a direct impact on the crystal growth rate.

The lattice parameters *a* and *c* of the samples was calculated using following equation (Rashad et al. 2015):

$$\frac{1}{d_{hkl}^2} = \frac{h^2 + k^2}{a^2} + \frac{l^2}{c^2} \tag{1}$$

where *a* and *c* are lattice parameters, d is the interplanar distance and *(h k l)* are the Miller indices.

It is clear that the values of cell parameters and lattice volumes of Eu^{2+}, R^{3+}-codoped samples are decreased than those of Eu^{2+}-doped sample of as a result of the shrinkage in the M–O bonds. This behavior could be explained by the differences of radius of substituted metal ions (i.e. $Sr^{2+} < R^{3+}$), which also certifies the measured reduction in the crystallite size of Eu^{2+}, R^{3+}-codoped samples. The variations in the crystallographic parameters and phases are collected in Table 1.

3.2 Crystal morphology

Figure 2 reveals the FE-SEM images of SMS1, SMS2, SMS3 and SMS4 phosphors at two different magnifications × 2000 (a, c, g, e) and × 5000 (b, d, f, h). The microstructure of Eu^{2+}-doped sample (SMS1) appears with hierarchical -like texture. The particles have spherical shape of fused interconnections and their size ranges from 1 to 3 µm. The second sample SMS2 displays sponge-like structure. The particle size average slightly decreases which encourages higher diffusion among the interconnected particles. However, the Tm^{3+} ion addition in the third sample SMS3 forms a homogenous surface of small agglomeration and regularly distributed pores. The particle size average ranges from 0.5 to 1.5 µm. Meanwhile, the fourth sample SMS4 indicated different particles shape and dimensions.

Table 1 Crystallographic properties of the $Sr_2MgSi_2O_7$ main phase in the as-prepared phosphor powders

As-prepared phosphors	Crystallite size (nm)	Lattice parameters (Å)		Cell volume (Å^3)	$Sr_2MgSi_2O_7$ phase	Sr_2SiO_4 phase	$SrSiO_3$ phase
		a	*c*				
SMS1	77.2	7.950408	5.122916	323.814	+	+	+
SMS2	70.6	7.94812	5.121443	323.535	+	+	+
SMS3	57.9	7.948585	5.121741	323.592	+	+	+
SMS4	22.5	7.945759	5.122808	323.429	+	+	+

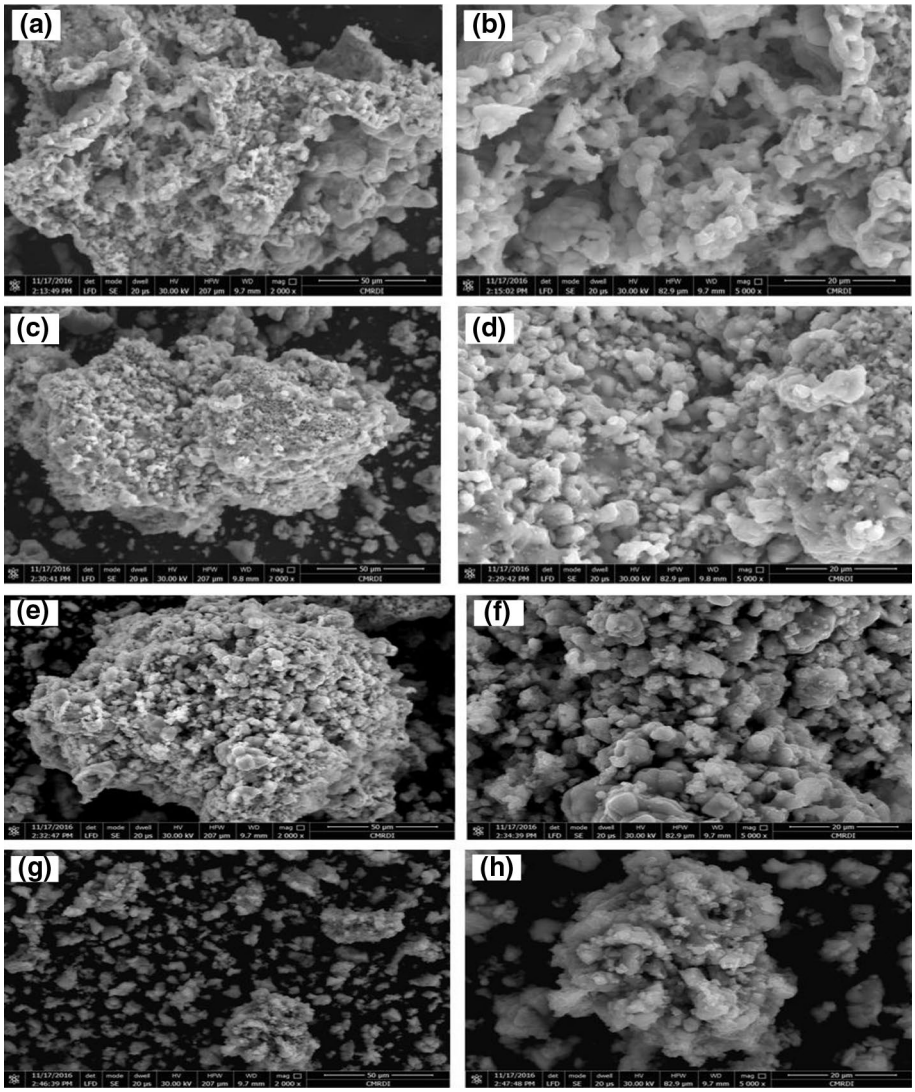

Fig. 2 FE-SEM micrographs of SMS1 (**a**, **b**), SMS2 (**c**, **d**), SMS3 (**e**, **f**) and SMS4 (**g**, **h**) phosphor powders

This could be assigned to the presence of mixed phases creating intrinsic allotropic like structure. Therefore, both the porosity and particle size average are clearly decreased in comparison with other samples. These obtained particle size results are found to be in a good agreement with the calculated crystallographic parameters from XRD data. The specific surface area S_{BET} was 10.138 m^2/g whereas the mean pore diameter and pore volume were 10.4129 nm and 5.27×10^{-3} cm^3/g, respectively Eu^{2+}-doped SMS1 sample phosphors calcined at 1200 °C for 3 h. The low surface area was attributed to the absorption of some organic species results from the combustion of urea on the surface of the samples (Rashad et al. 2016).

3.3 Optical properties

3.3.1 Diffuse reflectance and absorption spectra

The UV–Vis diffuse reflectance and absorption spectra of Eu^{2+}-doped and Eu^{2+}, R^{3+} (Er^{3+}, Tm^{3+} or Tb^{3+}) codoped samples calcined at 1200 °C for 3 h were displayed in Fig. 3. All samples was characterized by a relatively high reflectivity ~ 72% for sample SMS1 above 500 nm, and the highest was ~ 75% for sample SMS4 above 320 nm as shown in Fig. 3a. As clearly visible, the absorbance spectrum shows absorbance values of about 0.15 for samples SMS1 and SMS2, 0.13 at wavelengths above 500 nm as well as samples SMS3 and SMS4 as shown in Fig. 3b.

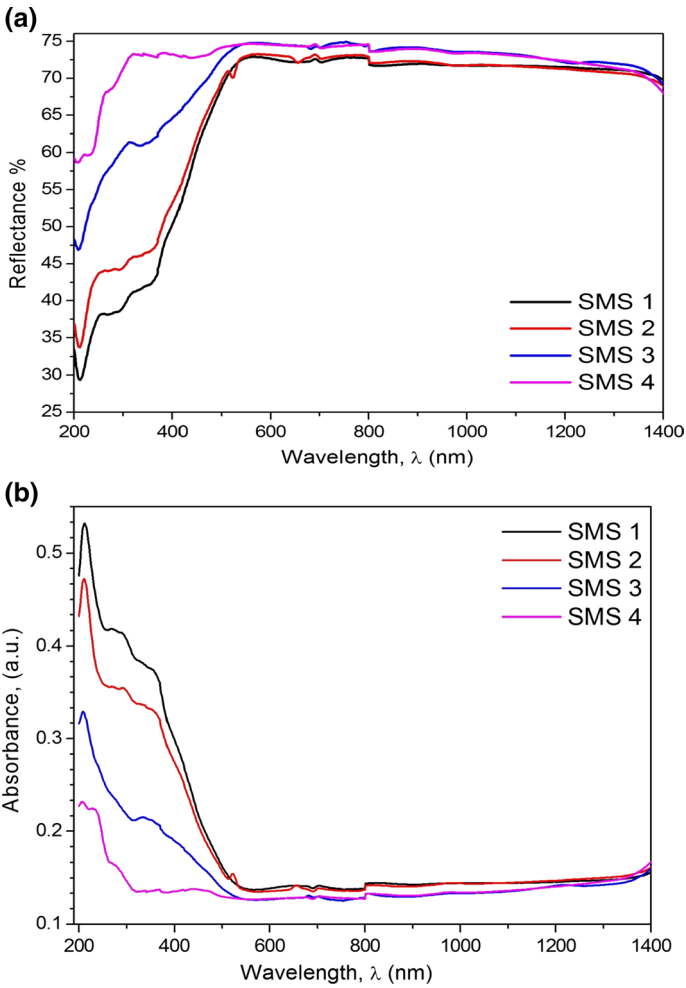

Fig. 3 UV-Vis **a** diffuse reflectance spectra and **b** absorption spectra of the as-synthesized phosphors

3.3.2 Band gap energy

In the limiting case of an infinitely powder samples, thickness and sample holder have no influence on the value of reflectance (R). In this case, the Kubelka–Munk equation at any wavelength becomes (Elseman et al. 2016):

$$F(R\infty) = K/S = (1-R)/(2R) \tag{2}$$

F ($R\infty$) is the so-called remission or Kubelka–Munk function which is proportional to absorption, S called K–M scattering and K absorption coefficients. In the parabolic band structure, the band gap Eg, and absorption coefficientα, of a direct band gap semiconductor are related through the well known equation (Sanad et al. 2016):

$$\alpha h\nu = A(h\nu - Eg)^{1/2} \tag{3}$$

where α is the linear absorption coefficient of the material, $h\nu$ is the photon energy and A is proportionality constant. When the material scatters in perfectly diffuse manner (or when it is illuminated at $60\pm$incidence), the K–M absorption coefficient (K) becomes equal to 2α ($K=2\alpha$). In this case, considering the K–M scattering coefficient (S) as constant with respect to wavelength, and using the remission function in Eq. (2) we obtain the expression (Elseman et al. 2016):

$$(h\nu F(R\infty))^2 = B(h\nu - Eg) \tag{4}$$

Therefore, obtaining F ($R\infty$) from Eq. (3) and plotting the $[F(R\infty)h\nu]^2$ against $h\nu$, the band gap E_g of a powder sample can be extracted easily. It is found that $Sr_{1.98}MgSi_2O_7$: $Eu^{2+}_{0.01}$, $Tm^{3+}_{0.01}$ sample posses the lowest E_g value among those of the other samples as illustrated in Fig. 4. For instance, it is also seen that the ionic radius of the rare earth dopants are in the following order [Tm^{3+} (230 pm) < Er^{3+} (232 pm) < Tb^{3+} (237 pm) < Eu^{2+} (240 pm)]. Therefore, our band gap energy measurements are in good agreement with the fact of increasing E_g value with decreasing ionic radius of doping ion and vices versa (Mote et al. 2013; Manikandan et al. 2013; Huse et al. 2013; Viswanath et al. 2014).

3.3.3 Refractive index and dielectric constant

The refractive index (n) of semiconducting materials is very important in determining the optical properties of the material. Knowledge of n is essential to design heterostructure lasers in the optoelectronic devices as well as in the solar cell applications.

The refractive index (n) of the samples can be calculated using Herve and Vandamme relation (Herve and Vandamme 1994). Where E_g is the energy band gap.

$$n = \sqrt{1 + \left(\frac{A}{E_g + B}\right)^2} \tag{5}$$

Where A and B are numerical constants with values of 13.6 and 3.4 eV, respectively. The calculated averages of the refractive index for Eu^{3+}-doped and R^{3+}, Eu^{3+}-doped samples are recorded in Table 2. Figure 5 evinces the variation in the refractive indices against the band gap energies. It is indicated that the minimum refractive index (***n***) was **1.93** at 4.82 eV for $Sr_{1.98}MgSi_2O_7$: $Eu^{2+}_{0.01}$, $Tm^{3+}_{0.01}$ sample. Moreover, it can also be implied that the refractive indices are shifted towards lower values at higher E_g values.

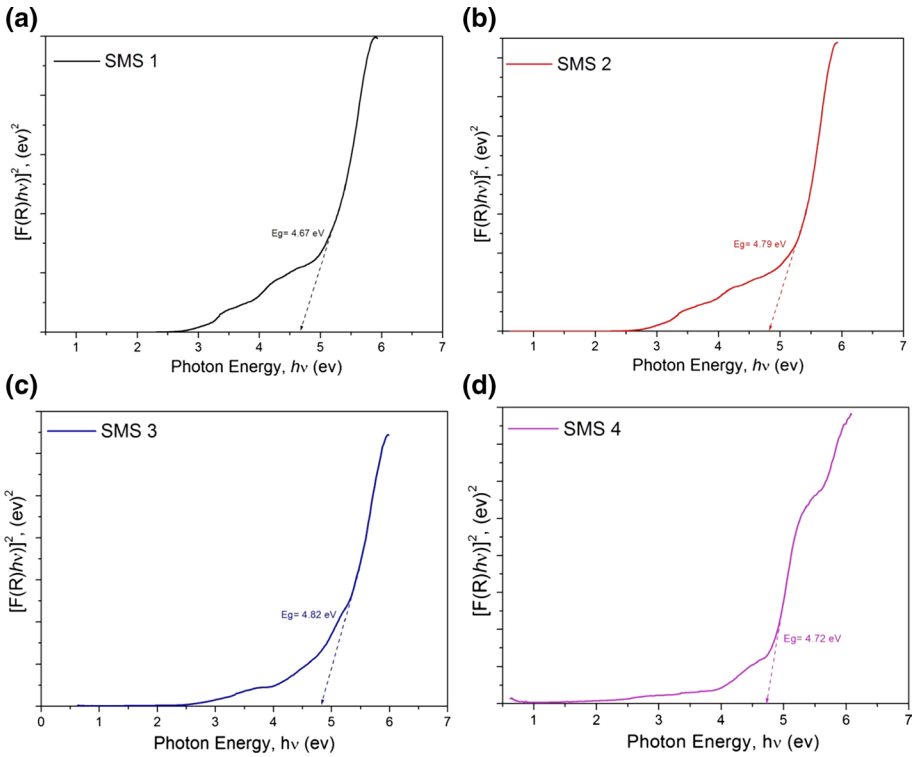

Fig. 4 Optical band gap energy of SMS1 (**a**), SMS2 (**b**), SMS3 (**c**) and SMS4 (**d**) phosphor powders

On the other hand, both static and high frequency dielectric constants are determined for all the samples as listed in Table 2. The high frequency dielectric constant (ε_α) is calculated using the relation (Herve and Vandamme 1994):

$$\varepsilon_\alpha = n^2$$

The static dielectric constant (ε_0) of the samples is calculated using the relation (Herve and Vandamme 1994):

$$\varepsilon_0 = 18.52 - 3.08E_g$$

Such obtained results emphasized that the change in the refractive indices and dielectric constants are mainly relied on the absorption features of these phosphors.

3.3.4 Photoluminescence (PL) properties

Figure 6 reveals the typical PL emission spectrum of the as-prepared phosphors after excitation at different wavelengths (365, 380, 390 and 410 nm). The PL results of SMS1 sample show two broad convoluted emission bands which are centered around 460 and 555 nm. The deconvolution of the bands increases with increasing excitation wavelength. The collected signals are different in the band width and intensity. The existence of two types of luminescent centers is due to the difference of coordination number of

Table 2 Effect of R^{3+} cations on the optical properties of Eu^{2+}-$Sr_2MgSi_2O_7$ phosphor powders

Phosphor sample	E_g (eV)	Refractive index (n)	ε_α	ε_0	Luminescent peaks centers wavelength (nm)				
					λ_{EM} *at* λ_{EX} = 365 nm	λ_{EM} *at* λ_{EX} = 380 nm	λ_{EM} *at* λ_{EX} = 390 nm	λ_{EM} *at* λ_{EX} = 410 nm	*FWHM* (nm)
SMS1	4.67	1.96	3.84	4.14	461.4, 554.3	460.4, 554.8	459.8, 552.7	457.1, 559.7	58
SMS2	4.79	1.94	3.76	3.77	462.5, 546.2	461.8, 549.5	460.6, 555.5	457.7, 560.2	67
SMS3	4.82	1.93	3.74	3.67	481.8, 549.7	477.5, 548.4	470.5, 552.6	454.5, 559.2	148
SMS4	4.72	1.95	3.81	3.98	449.6, 555.4	488.8, 538.7	486.6, 539.8	450.1, 551.2	133

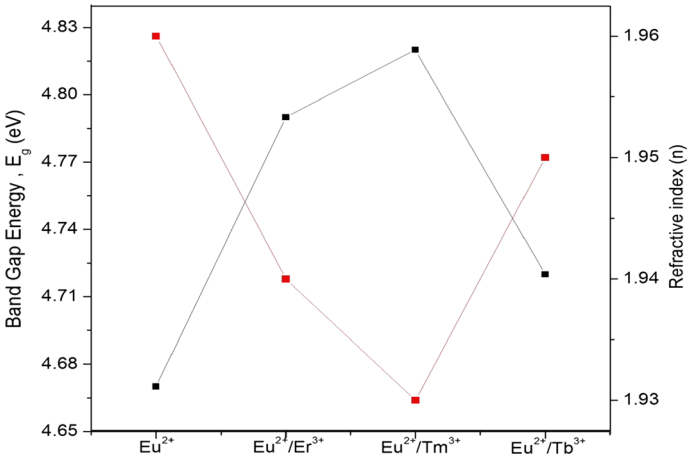

Fig. 5 Optical band gap energy and the calculated refractive indices of phosphors powders

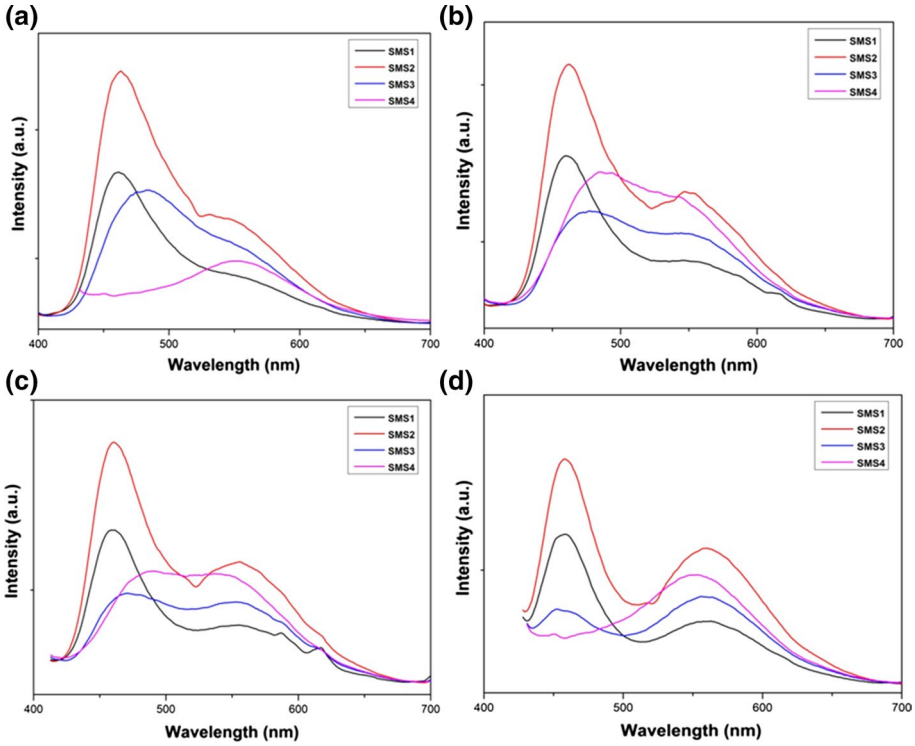

Fig. 6 PL emission spectra of all prepared phosphors at different excitation wavelengths **a** $\lambda_{Ex} = 365$ nm, **b** $\lambda_{Ex} = 380$ nm, **c** $\lambda_{Ex} = 390$ nm, **d** $\lambda_{Ex} = 410$ nm

Sr from 6 to 8 in the $Sr_2MgSi_2O_7$ crystal structure (He et al. 2010; Dutczak et al. 2012). Therefore, the Eu^{2+} ions replaces Sr^{2+} ion and located two different sites (Eu 1 and Eu 2) (Ochi 2006; Fei et al. 2005; Zhang et al. 2010). Consequently, the emission bands at 460 and 555 nm are attributed to the excitation transitions of different Eu^{2+} centers $4f^6$–$4f^15d^7$. The Eu^{2+} ion becomes an excited Eu^+ after the capture of the excited electrons in the conduction band. Meanwhile, the codopant ions R^{3+} (Er^{3+}, Tm^{3+} or Tb^{3+}) act as trap levels for the created free holes and turn into R^{4+}. After the termination of excitation source, the hole is thermally released to the valence band again and migrates to the excited Eu^+ ion where it is captured. As a result recombination takes place, i.e. the excited Eu^+ returns to the Eu^{2+} ground state, which gives rise to the persistent luminescence properties (Pan et al. 2008; Sabbagh Alvani et al. 2005; Shirakura et al. 2005). It is clear that the SMS1 showed higher performance than the reported results at the same excitation wavelengths (Song et al. 2008; Zhang et al. 2010). Meanwhile, SMS2, SMS3 and SMS4 samples displayed similar performance to the previous published co-doped phosphors (Pan et al. 2008; Jun et al. 2014).

Eventually, Er^{3+}, Eu^{2+}-codoped sample reveals the maximum intensity and broadening of PL emission peaks in comparison with other co-doped phosphors. This behavior could be explained by the largest ionic radii difference between Eu^{2+} and Er^{3+} ions which leads to creating the largest number of trapping and releasing effects, thus strong and weak emission bands are easily recorded (Sanad and Rashad 2016).

The PL emission spectrum at excitation $\lambda_{EX} = 380$ nm of Eu^{2+}-doped and Eu^{2+}, R^{3+} (Er^{3+}, Tm^{3+} or Tb^{3+}) co-doped samples annealed at 1200 °C for 3 h were displayed in Fig. 6b were seen Eu^{2+}-doped $Sr_{1.98}MgSi_2O_7$ (SMS1) at around 461 nm (2.69 eV) with a broad line shape with FWHM of 58 nm, whereas in Eu^{2+}, Er^{3+} doped (SMS2) it is seen at around 462 nm (2.68 eV) with FWHM of 67 nm, Eu^{2+}, Tm^{3+} (SMS3) it is seen at around 477 nm (2.60 eV) with FWHM of 148 nm and Eu^{2+}, Tb^{3+} (SMS4) it is seen at around 485 nm (2.56 eV) with FWHM of 133 nm, as listed in Table 2.

Figure 7 illustrates band deconvolution of the photoluminescence spectra of R^{3+} (Er^{3+}, Tm^{3+} or Tb^{3+}) co-doped $Sr_2MgSi_2O_7$:Eu^{2+} phosphor annealed at 1200 °C for 3 h. Figure 7a shows under the near UV excitation of 380 nm, deconvolution of $Sr_2MgSi_2O_7$:Eu^{2+} phosphor three broads blue emission band centered around 430–495 nm and several sharp lines in the orange–red region peaking at about 522, 592, 616, 632, and 658 nm. The broad blue emission band, it is known that Eu^{2+} presents three broads emission band peaking at around 430–495 nm due to the $4f\,5d^1$ to $4f^7$ transition of Eu^{2+}($^8S_{7/2}$-^7F_j, j = 0, 1, 2, 3, and 4) (Hao Tam et al. 2016). The red emission lines should be ascribed to the transitions within the $4f^6$ configuration of Eu^{3+} which these lines corresponds to the $^5D_0 \rightarrow {}^7F_0$, $^5D_0 \rightarrow {}^7F_1$, $^5D_0 \rightarrow {}^7F_2$, $^5D_0 \rightarrow {}^7F_3$ and $^5D_0 \rightarrow {}^7F_4$ transitions of Eu^{3+}, respectively (Hao Tam et al. 2016; Yao et al. 2011). It could be possible that, co-doping R^{3+} ions e.g. Er^{3+}, Tm^{3+} and Tb^{3+} considerably a small amount of Eu^{3+} ions and R^{3+} were decreased Eu^{2+} ions that leads to the blue emission which can diminish this ions transformation. It can also be seen from Fig. 7 that while the PL intensity of the red emissions increased with different rare earth co-doped R^{3+} (Er^{3+}, Tm^{3+} or Tb^{3+}), the peak position and the shape of the blue band change arbitrary with different rare earth doping. However, the blue emission bands related to Eu^{2+} ions is sensitive to the host lattice environment, the change of the blue emission band with different rare earth co-doped R^{3+} (Er^{3+}, Tm^{3+} or Tb^{3+}) may indicate the change of the crystalline phases in the sample as observed from XRD results. Furthermore, the increase of the PL intensity of the red emission is related to the higher content of the $Sr_2MgSi_2O_7$ phase upon to different rare earth co-doped R^{3+} (Er^{3+}, Tm^{3+} or Tb^{3+}).

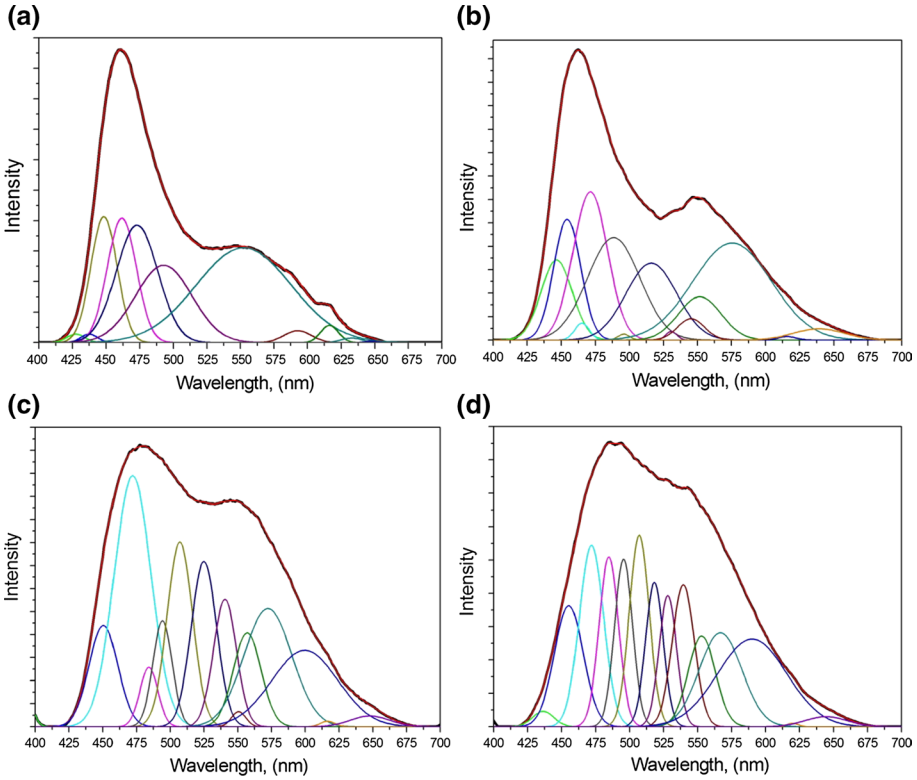

Fig. 7 The band deconvolution of PL ($\lambda_{ex}=380$ nm) spectra of **a** Eu^{3+}, **b** Eu^{3+},Er^{3+}, **c** Eu^{3+},Tm^{3+} or **d** Eu^{3+},Tb^{3+} co-doped $Sr_2MgSi_2O_7$:Eu^{2+} phosphor annealed at 1200 °C for 3 h

4 Conclusion

Different samples of lanthanides co-activated strontium magnesium silicate based phosphors have been successfully prepared using simple urea combustion technique. The changes in the crystal structure and the morphology of the formed particles have been investigated in the presence and the absence of trivalent co-doping ions including Er^{3+}, Tm^{3+} or Tb^{3+}. Clearly, tetragonal $Sr_2MgSi_2O_7$ phase was the dominant phase while Sr_2SiO_4 and $SrSiO_3$ were the minor phases with monoclinic crystal structures, respectively. FE-SEM results established the decrease of particle size with uniform microstructure with lanthanide co-doping were exhibited. Nevertheless, $Sr_{1.98}MgSi_2O_7$:$Eu^{2+}_{0.01}$ sample displayed the hierarchical sponge-like morphologies with the few interconnected particles. The $Sr_{1.99}MgSi_2O_7$:$Eu^{2+}_{0.01}$ sample demonstrated the minimum band gap energy ~ 4.67 eV, whereas $Sr_{1.98}MgSi_2O_7$:$Eu^{2+}_{0.01}$, $Tm^{3+}_{0.01}$ achieved the maximum band gap energy ~ 4.82 eV. The photoluminescence emission spectrum show two broad convoluted emission bands which were centered around 460 and 555 nm as well as the deconvolution of the bands raised with rising the excitation wavelength. Er^{3+}, Eu^{2+}-co-doped sample revealing the maximum intensity and broadening PL emission peaks in comparison with other co-doped phosphors.

References

Aitasalo, T., Hölsä, J., Laamanen, T., Lastusaari, M., Lehto, L., Niittykoski, J., Pellé, F.: Luminescence properties of Eu 2+ doped dibarium magnesium disilicate, Ba 2 MgSi 2 O 7: Eu 2+. Ceram.-Silikaty **49**, 58–62 (2005)

Aitasalo, T., Hölsä, J., Jungner, H., Lastusaari, M., Niittykoski, J.: Thermoluminescence study of persistent luminescence materials: Eu2+-and R3+-doped calcium aluminates, CaAl2O4: Eu2+, R3+. J. Phys. Chem. B **110**, 4589–4598 (2006)

Alvani, A.A.S., Moztarzadeh, F., Sarabi, A.A.: Preparation and properties of long afterglow in alkaline earth silicate phosphors co-doped by Eu2O3 and Dy2O3. J. Lumin. **115**, 147–150 (2005)

Bhatkar, V.B., Bhatkar, N.V.: Combustion synthesis and photoluminescence study of silicate biomaterials. Bull. Mater. Sci. **34**, 1281–1284 (2011)

Chen, Y., Liu, B., Kirm, M., Qi, Z., Shi, C., True, M., Vielhauer, S., Zimmerer, G.: Luminescent properties of blue-emitting long afterglow phosphors Sr2− xCax MgSi2O7: Eu2+, Dy3+ (x= 0, 1). J. Lumin. **118**, 70–78 (2006)

Clabau, F., Rocquefelte, X., Jobic, S.: Mechanism of phosphorescence appropriate for the long-lasting phosphors Eu2+-doped SrAl2O4 with codopants Dy3+ and B3+. Chem. Mater. **17**, 3904–3912 (2005)

Dorenbos, P.: Mechanism of persistent luminescence in Eu2+ and Dy3+ codoped aluminate and silicate compounds. J. Electrochem. Soc. **152**, H107–H110 (2005)

Dutczak, D., Milbrat, A., Katelnikovas, A., Meijerink, A., Ronda, C., Justel, T.: Yellow persistent luminescence of Sr2SiO4: Eu2+, Dy3+. J. Lumin. **132**, 2398–2403 (2012)

Elseman, A.M., Rayan, D.A., Rashad, M.M.: Structure, optical and magnetic behavior of nanocrystalline CuO nanopowders synthesized via a new technique using Schiff base complex. J. Mater. Sci. Mater. Electron. **27**, 2652–2661 (2016)

Fei, Q., Chang, C.K., Mao, D.L.: Luminescent properties of Sr2MgSi2O7 and Ca2MgSi2O7 long lasting phosphors activated by Eu2+, Dy3+. J. Alloys Compd. **390**, 133–137 (2005)

Fu, Z.L., Zhou, S.H., Zhang, S.Y.: Study on optical properties of rare-earth ions in nanocrystalline monoclinic SrAl2O4: Ln (Ln= Ce3+, Pr3+, Tb3+). J. Phys. Chem. B **109**, 14396–14400 (2005)

Gong, Y., Xu, X.H., Zeng, W., Wu, C.J., Wang, Y.H.: Ce^{3+}, Mn^{2+} Co-doped red-light long-lasting phosphor: $BaMg_2Si_2O_7$ through energy transfer. Phys. Proced. **29**, 86–90 (2012)

Hao Tam, T.T., Hung, N.D., Lien, N.T.K., Kien, N.D.T., Huy, P.T.: Synthesis and optical properties of red/blue-emitting Sr2MgSi2O7: Eu3+/Eu2+ phosphors for white LED. J. Sci. Adv. Mater. Devices **1**, 204–208 (2016)

He, H., Fu, R., Song, X., Li, R., Pan, Z., Zhao, X., Deng, Z., Cao, Y.: Observation of fluorescence and phosphorescence in Ca2MgSi2O7: Eu2+, Dy3+ phosphors. J. Electrochem. Soc. **157**, J69–J73 (2010)

Herve, P., Vandamme, L.K.J.: General relation between refractive index and energy gap in semiconductors. Infrared Phys. Technol. **35**, 609–615 (1994)

Huse, V.R., Mote, V.D., Dole, B.N.: The crystallographic and optical studies on cobalt doped CdS nanoparticles. World J. Condens. Matter Phys. **3**, 46–49 (2013)

Ishizaki, M., Odawara, O., Katagiri, T., Sasagawa, T., Wada, H., Kitamoto, Y.: Preparation of SiO_2-capped $Sr_2MgSi_2O_7$: Eu, Dy nanoparticles with laser ablation in liquid. J. Nanotechnol. **2012**, 435205 (2012)

Jun, L., Qiang, G., Kaiyan, Z., Mingqiao, G., Jialin, L.: Structure and luminescent properties of luminous polypropylene fiber based on Sr2MgSi2O7: Eu2+, Dy3+. J. Rare Earth **32**, 696–701 (2014)

Li, Y., Wang, Y., Xu, X., Gong, Y.: Effects of non-stoichiometry on crystallinity, photoluminescence and afterglow properties of Sr2MgSi2O7: Eu2+, Dy3+ phosphors. J. Lumin. **129**, 1230–1234 (2009)

Liu, B., Shi, C., Yin, M., Dong, L., Xiao, Z.: The trap states in the Sr2MgSi2O7 and (Sr, Ca) MgSi2O7 long afterglow phosphor activated by Eu2+ and Dy3+. J. Alloys Compd. **387**, 65–69 (2005)

Maldiney, T., Viana, B., Bessière, A., Gourier, D., Bessodes, M., Scherman, D., Richard, C.: In vivo imaging with persistent luminescence silicate-based nanoparticles. Opt. Mater. **35**, 1852–1858 (2013)

Manikandan, A., Vijaya, J.J., Sundararajan, M., Meganathan, C., Kennedy, L.J., Bououdina, M.: Optical and magnetic properties of Mg-doped ZnFe2O4 nanoparticles prepared by rapid microwave combustion method. Superlattices Microstruct. **64**, 118–121 (2013)

Mote, V.D., Dargad, J.S., Dole, B.N.: Effect of Mn doping concentration on structural, morphological and optical studies of ZnO nano-particles. Nanosci. Nanoeng. **1**, 116–122 (2013)

Ochi, Y.: Crystal structure of Sr-akermanite glass–ceramics. Mater. Res. Bull. **41**, 1825–1834 (2006)

Pan, W., Ning, G., Zhang, X., Wang, J., Lin, Y., Ye, J.: Enhanced luminescent properties of long-persistent Sr2MgSi2O7: Eu2+, Dy3+ phosphor prepared by the co-precipitation method. J. Lumin. **128**, 1975–1979 (2008)

Rashad, M.M., Soltan, S., Ramadan, A.A., Bekheet, M.F., Rayan, D.A.: Investigation of the structural, optical and magnetic properties of CuO/CuFe2O4 nanocomposites synthesized via simple microemulsion method. Ceram. Int. **41**, 12237–12245 (2015)

Rashad, M.M., Mostafa, A.G., Rayan, D.A.: Structural and optical properties of nanocrystalline mayenite Ca 12 Al 14 O 33 powders synthesized using a novel route. J. Mater. Sci. Mater. Electron. **27**(3), 2614–2623 (2016)

Sabbagh Alvani, A.A., Moztarzadeh, F., Sarabi, A.A.: Effects of dopant concentrations on phosphorescence properties of Eu/Dy-doped Sr3MgSi2O8. J. Lumin. **114**, 131–136 (2005)

Sanad, M.M.S., Rashad, M.M.: Tuning the structural, optical, photoluminescence and dielectric properties of Eu 2+-activated mixed strontium aluminate phosphors with different rare earth co-activators. J. Mater. Sci. Mater. Electron. **27**, 9034–9043 (2016)

Sanad, M.M.S., Rashad, M.M., Abdel-Aal, E.A., El-Shahat, M.F., Powers, K.: Optical and electrical properties of Y 3+ ion substituted orthorhombic mullite Y (x) Al (6− x) Si 2 O 13 nanoparticles. J. Mater. Sci. Mater. Electron. **25**, 2487–2493 (2014)

Sanad, M.M.S., Rashad, M.M., Shenouda, A.Y.: Novel CuIn1-xGaxTe2 structures for high efficiency photoelectrochemical solar cells. Int. J. Electrochem. Sci. **11**, 4337–4351 (2016)

Shi, C.S., Fu, Y.B., Liu, B., Zhang, G.B., Chen, Y.H., Qi, Z.M., Luo, X.X.: The roles of Eu2þ and Dy3þ in the blue longlasting phosphor Sr2MgSi2O7: Eu2þ, Dy3þ. J. Lumin. **122**(123), 11–13 (2007)

Shirakura, S., Toda, K., Imanari, Y., Nonogawa, T., Uematsu, K., Sato, M., Nishisu, Y., Kobayashi, M.: Sol-gel synthesis of long persistent phosphor Sr 2 MgSi 2 O 7: Eu, Dy thin film. J. Ceram. Soc. Jpn. **113**, 484–487 (2005)

Song, F., Donghua, C., Yuan, Y.: Synthesis of Sr2MgSi2O7: Eu, Dy and Sr2MgSi2O7: Eu, Dy, Nd by a modified solid-state reaction and their luminescent properties. J. Alloys Compd. **458**, 564–568 (2008)

Viswanath, R., Naik, H.S.B., Somalanaik, Y.K.G., Neelanjeneallu, P.K.P., Harish, K.N., Prabhakara, M.C.: Studies on characterization, optical absorption, and photoluminescence of yttrium doped ZnS nanoparticles. J. Nanotechnol. **2014**, 924797 (2014)

Wu, H., Hu, Y., Wang, Y., Zeng, B., Mou, Z., Deng, L.: Influence on luminescent properties of the Sr2MgSi2O7: Eu2+ by Dy3+, Nd3+ co-doping. J. Alloys Compd. **486**, 549–553 (2009)

Wu, H.Y., Hu, Y.H., Wang, Y.H., Fu, C.J.: The luminescent properties of the substitution of Ho3+ for Dy3+ in the M2MgSi2O7: Eu2+, Dy3+ (M: Sr, Ca) long afterglow phosphors. Mater. Sci. Eng. B **172**, 276–282 (2010a)

Wu, H., Hu, Y., Wang, Y., Fu, C.: Influence on the luminescence properties of the lattice defects in Sr2MgSi2O7: Eu2+, M (M= Dy3+, La3+ or Na1+). J. Alloys Compd. **497**, 330–335 (2010b)

Wu, B.Y., Wang, H.F., Chen, J.T., Yan, X.P.: Fluorescence resonance energy transfer inhibition assay for α-fetoprotein excreted during cancer cell growth using functionalized persistent luminescence nanoparticles. J. Am. Chem. Soc. **133**, 686–688 (2011a)

Wu, H., Hu, Y., Zeng, B., Mou, Z., Dengunable, L.: Tunable luminescent properties by adjusting the Sr/Ba ratio in Sr1. 97− xBaxMgSi2O7: Eu2+ 0.01, Dy3+ 0.02 phosphors. J. Phys. Chem. Solids **72**, 1284–1289 (2011b)

Yao, S., Xue, L., Yan, Y.: Luminescent properties of Sr 2 ZnSi 2 O 7: Eu 2+ phosphors prepared by combustion-assisted synthesis method. J. Electroceram. **26**, 112–115 (2011)

Ye, F., Dong, S., Tian, Z., Yao, S., Zhou, Z., Wang, S.: Fabrication of the PLA/Sr2MgSi2O7: Eu2+, Dy3+ long-persistent luminescence composite fibers by electrospinning. Optic. Mater. **36**, 463–466 (2013)

Yu, X.B., Zhou, C.L., He, X.H.: The influence of some processing conditions on luminescence of SrAl2O4: Eu2+ nanoparticles produced by combustion method. Mater. Lett. **58**, 1087–1091 (2004)

Zhang, X., Tang, X., Zhang, J., Wang, H., Shi, J., Gong, M.: Luminescent properties of Sr2MgSi2O7: Eu2+ as blue phosphor for NUV light-emitting diodes. Powder Technol. **204**, 263–267 (2010)